Materials Advances

ROYAL SOCIETY OF CHEMISTRY

PAPER

View Article Online
View Journal

Cite this: DOI: 10.1039/d6ma00515b

In situ grown synergistic Co-based metal–organic framework/graphene oxide composite for enhanced supercapacitor performance

Soumen Khan, *[ab] K. Padmasri,[c] Unmesha Mondal[a] and Chanchal Chakraborty *[ab]

Received 13th April 2026,
Accepted 27th May 2026

DOI: 10.1039/d6ma00515b

rsc.li/materials-advances

The use of pristine metal–organic frameworks (MOFs) as active electrodes for energy storage is challenging in practice due to their low conductivity and electrochemical durability. To increase the energy storage performance of the pristine MOF, an *in situ* graphene oxide (GO) composite of a cobalt succinate MOF (abbreviated as Co-MOF) is designed using cheap, commercially available starting materials for an energy storage electrode. Herein, we demonstrate the MOF-GO composites with GO weight percentages of 5% (Co-MOF-GO5) and 10% (Co-MOF-GO10) to elucidate the potential of these composites for high-performance supercapacitors. Among them, Co-MOF-GO5 exhibits the highest specific capacitance of 552 F g^{-1}, with excellent cycle stability over 5000 cycles and improved energy density (33 W h kg^{-1}) and power density (2.9 kW kg^{-1}) in a three-electrode cell system compared with those of pristine Co-MOF and other composites. The calculated electrochemically active surface area (ECSA) and lower charge transfer resistance also support the better performance of Co-MOF-GO5 compared with Co-MOF-GO10. To assess the practical applicability of Co-MOF-GO5 as an energy storage material, symmetric CR2032 coin-cell devices were fabricated using Co-MOF-GO5 at both electrodes with an aqueous KOH electrolyte. These devices can power a commercially available light-emitting diode bulb (~1.8 V) for a few minutes.

1. Introduction

The rapid exhaustion of fossil fuels, amid rising environmental and geopolitical concerns, has increased the demand for sustainable and effective energy storage solutions.[1–3] Renewable sources, like wind and solar energy, are promising alternatives, but their intermittent nature poses challenges for grid reliability. As a result, advanced energy storage systems capable of delivering high power and long-term durability are required to overcome the recent energy crisis.[4,5] Among the accessible technologies, like supercapacitors (SCs), conventional capacitors, batteries, and fuel cells, SCs have appeared as striking candidates owing to their rapid charge–discharge ability, high power and energy density, long-term cyclability, and safety in operation.[6–10] However, their comparatively low energy density compared with that of batteries remains a main limitation, which can be addressed by the judicious design of electrode materials for SCs.[11–13]

Active electrode materials play a pivotal role in determining the electrochemical performance of SCs. To date, a variety of materials, including carbon materials, transition-metal-based oxides or hydroxides, and conducting polymers, have been widely studied in this regard.[14,15] Carbon-based materials offer excellent electrical conductivity and cycling durability, but they typically store charge only through electric double-layer capacitance (EDLC), which results in a limited energy density.[16,17] On the other hand, redox-active metal oxides or conducting polymers exhibit high capacitance *via* faradaic redox reactions, known as pseudocapacitance systems, which provide better energy density, but these systems may often suffer from poor cyclability and low rate capability.[18,19] Therefore, the rational design of hybrid electrode materials, which can integrate the EDLC and pseudocapacitive contributions, has become a widely adopted approach for overcoming these intrinsic limitations.[20–24]

From this perspective, metal–organic frameworks (MOFs) have recently attracted substantial attention as next-generation electrode materials for sustainable energy storage and conversion systems.[25–30] MOFs are porous crystalline materials with

[a] Department of Chemistry, Birla Institute of Technology & Science (BITS) Pilani, Hyderabad Campus, Jawaharnagar, Samirpet, Hyderabad, Telangana, 500078, India. E-mail: p20220015@hyderabad.bits-pilani.ac.in, chanchal@hyderabad.bits-pilani.ac.in

[b] Materials Center for Sustainable Energy & Environment (McSEE), Birla Institute of Technology & Science (BITS) Pilani, Hyderabad Campus, Jawaharnagar, Samirpet, Hyderabad, Telangana, 500078, India

[c] Department of Chemical Engineering, Birla Institute of Technology and Science-Pilani, Hyderabad Campus, Jawaharnagar, Samirpet, Hyderabad, Telangana, 500078, India

high surface areas in which metal ions or clusters are coordinated to organic ligands, offering structural tunability to manipulate surface areas, pore sizes, and the abundance of redox-active metal centers.[31–34] All these unique structural features make MOFs fascinating candidates for SC-based energy storage electrodes, combining high surface-area EDLC and redox-based pseudocapacitive charge storage *via* the reversible redox reactions at the metal/ligand centers.[35–38] Nevertheless, the practical application of pristine MOFs in sustainable supercapacitors is severely hindered by their low intrinsic electrical conductivity and moderate structural stability under different electrochemical conditions during redox processes.[39,40] Keeping all of these in perspective, significant efforts have been made to develop MOF-based composites integrated with carbon-based materials, such as graphene oxide (GO), carbon nanotubes, reduced graphene oxide, metal nanoparticles or conducting polymers.[39,41–44] Among these materials, GO stands out owing to its large specific surface area, oxygen-containing functional groups, exceptional mechanical flexibility, and strong interfacial interactions with MOF frameworks.[39,40] GO not only enhances the charge transfer process but also suppresses particle accumulation, facilitating better ion diffusion and improving electrode/electrolyte wettability.[41–44] Remarkably, the growth of MOFs on GO sheets is more effective than physical mixing, as it enables close interfacial contact, structural reliability, and long-term electrochemical durability by preventing component separation during charging–discharging cycles.

Cobalt-based MOFs have attracted particular attention for SC applications owing to the rich redox chemistry of the Co^{2+}/Co^{3+} couple, which can provide high pseudocapacitive contributions.[45–48] Although reports on cost-effective, environmentally friendly cobalt-carboxylate MOFs with carbon-based materials, like GO, are available in the literature, their rational integration with graphene oxide *via* an *in situ* synthesis process to improve interfacial contact remains highly desirable. In addition, systematic research correlating GO content with electrochemical performance is crucial to identify optimal compositions that balance conductivity enhancement with ion-accessible active metal sites.[39] Herein, we report a one-pot nimble *in situ* synthesis approach for GO-integrated Co-MOF (Co-MOF-GO) composites using cheap and commercially accessible precursors. By carefully tuning the GO content (5 and 10 wt%), we reveal that the optimized Co-MOF-GO5 composite exhibits better electrochemical performance than the pristine Co-MOF and other composite counterparts. The synergistic interface between the redox-active Co-MOF and GO sheets results in improved charge transport, faster ion diffusion, higher electrochemically active surface area (ECSA), reduced internal resistance, and superior cycling durability.[39] Additionally, the practical application of the improved electrode is authenticated through the fabrication of a symmetric CR2032 coin-cell SC capable of powering a commercial LED. This work provides valuable insights into the *in situ* composite formation of MOF/GO to enhance the energy storage performance through synergistic interfacial coupling, enabling cost-effective supercapacitor systems.

The actual uniqueness of this work lies in the selection of a non-aromatic, simple aliphatic dicarboxylate linker (succinate), inexpensive, commercially accessible precursors, and a water-mediated synthesis route, resulting in lower synthetic complexity, better scalability, lower cost, and a greener synthesis pathway. The *in situ* growth strategy enables intimate heterointerfacial contact between the cobalt succinate framework and GO nanosheets, unlike conventional physically mixed composites. The enhanced performance arises from the cooperative coupling of diffusion-controlled pseudocapacitance from Co-redox centres, surface EDLC contribution from GO, and interfacial charge-transfer synergy, which influence each other's structural and electrochemical stabilisation.

2. Experimental section

2.1. Materials

All chemicals and reagents were obtained from commercial vendors and used exactly as supplied. Sigma-Aldrich and Sisco Research Laboratories (SRL) Pvt. Ltd. in India provided cobalt chloride hexahydrate ($CoCl_2{\cdot}6H_2O$), succinic acid, potassium hydroxide (KOH), Nafion, carbon black, ethanol, methanol, sulphuric acid (H_2SO_4), graphite powder, sodium nitrite ($NaNO_2$), potassium permanganate ($KMnO_4$), hydrogen peroxide (H_2O_2), potassium iodide (KI), ammonia, and other solvents. Deionized water was used to prepare the KOH electrolyte solution for the electrochemical analysis. GRS Corporation, India, delivers nickel foam (width $\leq$1000 mm and thickness $\leq$2.5 mm). GO was synthesized as described in our previous study.[48]

2.2. Synthesis of Co-MOF

Co-MOF was synthesized using a previously reported procedure.[48–51] In a 100 mL beaker, 4 g (33.87 mmol) of succinic acid and 3.8 g (67.74 mmol) of KOH were added. To this, about 15 mL of water was added, followed by sonication for 15 minutes to dissolve the material and obtain a clear solution (solution A). The solution was then transferred to a 100 mL round-bottom (RB) flask. In another beaker, 8.33 g (35 mmol) of cobalt chloride ($CoCl_2{\cdot}6H_2O$) and 10 mL of water were added, followed by sonication for 15 min to obtain a clear solution, designated as solution B. Then, solution B was added dropwise to solution A with continuous stirring. After complete addition, the solution was refluxed at 110 °C for 24 hours to provide crystalline Co-MOF with a 90% yield.

2.3. Synthesis of Co-MOF/GO composites

To synthesize Co-MOF-GO5, first, 416 mg of GO (5 wt% with respect to the metal salt) was dispersed in 100 mL of distilled water and sonicated for 3 h. Then, the GO dispersion was allowed to stand for 1 h and sonicated for another hour. Finally, in the GO solution, 4 g (33.87 mmol) of succinic acid and 3.8 g (67.74 mmol) of KOH were added to the solution. To this, about 15 mL of water was added, followed by sonication for 15 minutes to obtain a clear solution (solution A). The solution was then transferred to a 100 mL RB flask. In another beaker, 8.33 g

(35 mmol) of $CoCl_2{\cdot}6H_2O$ and 10 mL of water were added, followed by sonication for 15 min to obtain a clear solution, designated as solution B. Then, solution B was added dropwise to solution A under continuous stirring. After the complete addition of solution B to solution A, the mixture was refluxed at 110 °C for 24 hours to yield the Co-MOF-GO5 composite. The 10 wt% GO composite (with respect to the metal salt), Co-MOF-GO10, was synthesized using a similar procedure.

2.4. General physicochemical characterization tools

The FTIR spectra of the Co-MOF and Co-MOF-GO composites were recorded in the ATR mode in the range of 4000–500 cm^{-1} using a Bruker-Alpha-II-Platinum ATR. UV-vis spectroscopic studies were carried out using a JASCO V-670 spectrometer. PXRD data were recorded using a Rigaku Ultima IV X-ray diffractometer for all the samples under constant parameters. Field-emission scanning electron microscopy (FESEM) and energy-dispersive X-ray analysis (EDX) of the drop-cast samples on a silicon wafer were performed using an FEI Apreo FESEM instrument at 20 kV. The thermal stability of the samples was analyzed using a Shimadzu DTG-60 TGA instrument over the temperature range of 30 °C to 800 °C at a heating rate of 10 °C min^{-1} under a N_2 atmosphere.

2.5. Electrochemical measurements

Pretreated Ni-foams were used for the electrochemical analysis of Co-MOF and its composites. The 10 mg Co-MOF or its composites were dispersed in 1 mL of DMF and mixed with 10 μL of Nafion and 1 mg of carbon black to form a slurry, which was then cast onto a Ni-foam (1 × 1 cm) electrode and dried in a vacuum oven at 60 °C for the study. The mass loading of Co-MOF is 0.5 mg cm^{-2}.

Electrochemical analyses, such as cyclic voltammetry (CV), galvanostatic charge–discharge (GCD), and electrochemical impedance spectroscopy (EIS) of the synthesized electrode materials, were performed in a three-electrode system using an OrigaFlex OGF500 electrochemical workstation. 1 M KOH was used as the electrolyte for all the experiments, Ag/AgCl as the reference electrode, and a Pt wire as the counter electrode. Ni foam was used as the current collector here. Electrochemical impedance spectroscopy (EIS) was performed over a frequency range of 1 Hz to 1 kHz using AC perturbation.

2.6 Determination of energy storage parameters

The gravimetric capacitance (C_g) determined from the constant current discharge curves was calculated using the following equation:[20,37,48,50,51]

$$C_g = \frac{I \times \Delta t}{m \times \Delta V}(\mathrm{F\ g^{-1}}), \quad (1)$$

where C_g (F g^{-1}) is the gravimetric capacitance, Δt is the discharge time (s) determined from the GCD study, V is the potential window (V), I is the constant current used for charging and discharging (mA), and m is the active mass of the material on one Ni-foam electrode exposed to the electrolyte (mg). The gravimetric energy density (ED) and power density (PD) are calculated using the following equations:

$$\mathrm{ED}\left(\frac{\mathrm{W\ h}}{\mathrm{kg}}\right) = \frac{C_g \times \Delta V^2}{2 \times 3.6}(\mathrm{W\ h\ kg^{-1}}), \quad (2)$$

$$\mathrm{PD}\left(\frac{\mathrm{W}}{\mathrm{kg}}\right) = \frac{\mathrm{ED}}{\Delta t} \times 3600\ (\mathrm{W\ kg^{-1}}) \quad (3)$$

The coulombic efficiency (η) was evaluated using the following equation:

$$\eta = \frac{t_d}{t_c} \times 100\%, \quad (4)$$

where t_d is the discharging time and t_c is the charging time. The following equation was used to calculate the equivalent series resistance (ESR):

$$\mathrm{ESR} = \frac{V_{drop}}{2I}, \quad (5)$$

where V_{drop} is the voltage drop at the beginning of the discharge curve and I is the discharge current. To investigate the real-world applicability of the synthesized Co-MOF-GO composite electrode material for energy storage, a symmetric CR2032 coin-cell-based supercapacitor configuration was developed with similar mass loadings of active materials on Ni-foam current collectors on both sides.

3. Results and discussion

The crystal structure of cobalt succinate tetrahydrate, $[Co(H_2O)_4(suc)]$, is well known and structurally similar to those of its complementary MOFs with Ni, Fe, Mg, and Mn.[48,49] In contrast to previous studies that relied on slow solvent evaporation, a straightforward, environmentally friendly synthetic method is employed here to prepare the Co-based MOF. Structural investigation reveals that the Co(II) center adopts an octahedral coordination environment coordinated by two oxygen atoms from the succinate ligands and four water molecules.[48,49] The succinate ligands occupy the axial positions, while the water molecules are arranged in the equatorial plane (Fig. 1a). Each succinate-coordinated cobalt(II) centre can be labelled by the empirical coordination environment of AB_2M_4. The succinate ligand binds through its two carboxylate groups in a monodentate manner, each coordinating to cobalt centres and extending the structure into a one-dimensional chain. Furthermore, the strong hydrogen bond between the coordinated water molecules and the carboxylate groups links adjacent chains, causing slight geometric distortion and contributing to overall structural durability.

To enhance the EDLC contribution, graphene oxide is incorporated into the MOF through synthesis (Fig. 1b).[39] GO was synthesized from graphite powder according to our previous report.[48] By changing the GO wt% (5% and 10% with respect to the metal wt%), two *in situ* MOF-GO composites were synthesized using the hydrothermal process, abbreviated as Co-MOF-GO5 and Co-MOF-GO10 (Fig. 1c). It is noteworthy that the *in situ* grown nanocomposites are superior compared to

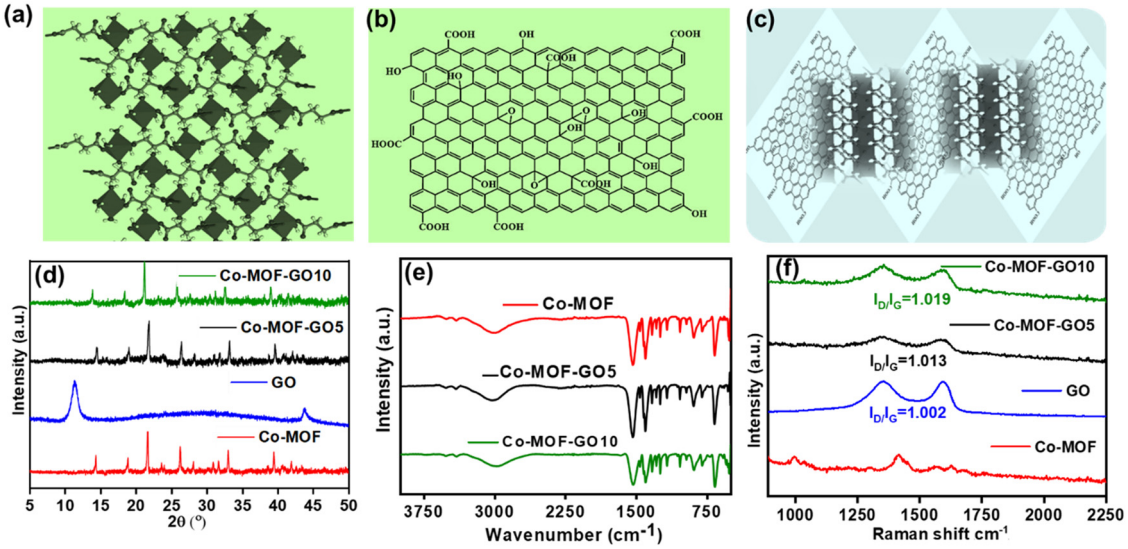

Fig. 1 (a) Packing diagrams of Co-MOF and (b) a layer of GO. (c) Plausible interaction image of the Co-MOF-GO composites. (d) PXRD patterns of the as-synthesized Co-MOF with GO and various wt% GO composites. (e) FT-IR spectra of Co-MOF, Co-MOF-GO5 and Co-MOF-GO10. (f) Raman spectra of Co-MOF, GO, Co-MOF-GO5, and Co-MOF-GO10.

physical mixing, as they can provide improved integrated systems with better interfacial coupling in a homogeneous composite.[39]

The phase transparency of the synthesized Co-MOF and its GO composites was assessed using a PXRD study (Fig. 1d). The Co-MOF diffraction pattern was collected over the 2θ range of 5°–45°, showing excellent agreement in peak locations with the referenced PXRD pattern of the compound, confirming the effective construction and high phase purity of the Co-MOF.[48–51] The functional groups present in the Co-MOF and its composites are confirmed by FTIR analysis, as shown in Fig. 1e. A broad peak observed at 3500–3000 corresponds to the presence of water molecules in Co-MOF. The small, narrow peak for ν(O–H) at 3521 is attributed to strong hydrogen bonds. The peaks at 1532, 1403, and 1243 cm^{-1} are attributed to carboxylate ions, O–H bending, and C–O, respectively, confirming coordination with the organic ligand. The ν as(C–C) stretching was observed at 1174 cm^{-1}.[48] The Raman spectra of Co-MOF, GO, and their composites are shown in Fig. 1f, which clearly reveal two distinct peaks at 1351 and 1595 cm^{-1}, corresponding to the typical D (defect and disorder) and G (graphitic) bands of the samples, respectively. The Raman spectrum intensity ratios of these bands (I_D/I_G) generally indicate the degree of structural disorder and the intensity of the defects. The I_D/I_G ratios were determined to be 1.013 and 1.019 for Co-MOF-GO5 and Co-MOF-GO10, respectively. The I_D/I_G values indicate the presence of more defect sites (sp^3) in the Co-MOF-GO10 structure than in Co-MOF-GO5. Raman analysis indicates higher graphitic ordering, greater electrical conductivity, and easier electron transfer in Co-MOF-GO5 than in Co-MOF-GO10, suggesting that a higher energy storage capacity can be achieved in Co-MOF-GO5. The features below 1000 cm^{-1} in the Raman spectra of Co-MOF reveal the vibrations for Co–O coordination at ~480 cm^{-1}, Co–O coupled mode with O–C–O at 640 cm^{-1}, coupled C–C/C–O vibrational mode of the coordinated succinate ligand influenced by Co–O bonding at 875 cm^{-1}, and C–C stretching at ~1000 cm^{-1}, as shown in Fig. S1 in the SI.

Morphological analysis by FESEM reveals clear modifications that directly correlate with supercapacitor performance. Pristine Co-MOF shows well-defined polyhedral particles containing smooth surfaces, while GO displays an archetypal, layered, and wrinkled nanosheet morphology (Fig. 2a and b). In the Co-MOF-GO5 composite, the Co-MOF particles are homogeneously distributed and firmly attached to the GO sheets, forming a uniform, porous structure (Fig. 2c). A well-integrated homogeneous morphology can provide many electrochemically active sites, narrow ion diffusion pathways, and efficient electron transport, leading to enhanced capacitive performance. On the other hand, Co-MOF-GO10 exhibits a denser morphology, with fractional restacking of GO sheets and accumulation of Co-MOF particles resulting from the higher GO content (Fig. 2d), which may block active sites and hinder electrolyte diffusion. The thermal stability of the synthesized Co-MOF, GO, and their composites was studied using fine-powder samples in the temperature range from 30 °C to 800 °C under a N_2 atmosphere, as shown in Fig. S2 in the SI. Initial ~28% weight loss at ~120 °C may be attributed to the exclusion of all four coordinated water molecules, and the second round of weight loss (~35%) near 400 °C–450 °C can be attributed to the degradation of the organic ligand.

The prime assessment of the electrochemical properties of Co-MOF and their GO composites was conducted in a three-electrode system, where a Ni-foam current collector loaded with the MOF or MOF-GO composite-based materials was used as the working electrode (WE), Ag/AgCl in saturated KCl was used as the reference electrode (RE), a Pt-wire was used as the counter electrode (CE), and 1 M KOH was used as the electrolyte.[51–55] The applied potential window of the working electrode was assessed by anodically cyclic scanning from 0 to 0.47 V (*vs.* Ag/AgCl),

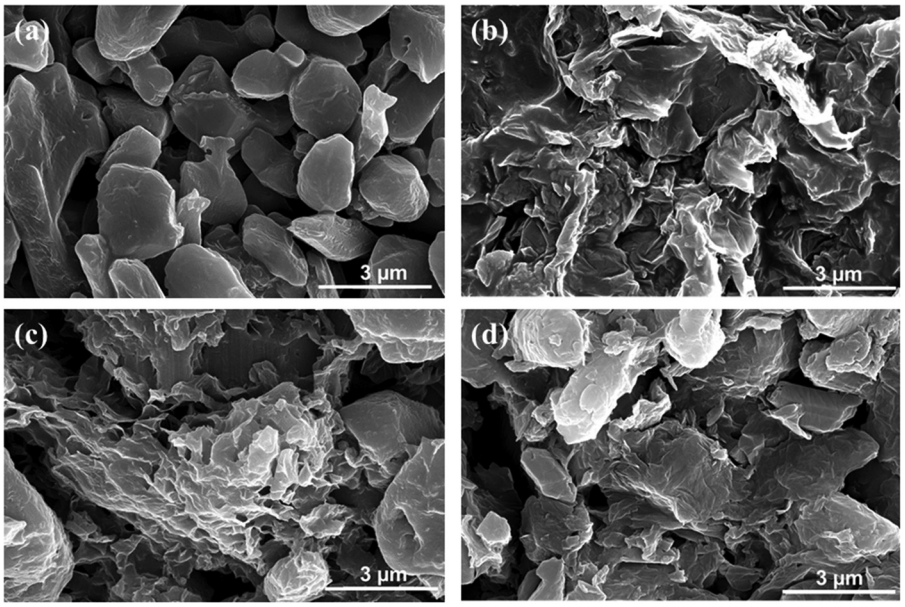

Fig. 2 FESEM images of (a) Co-MOF, (b) GO, (c) Co-MOF-GO5, and (d) Co-MOF-GO10.

providing the reversible redox peaks of Co^{2+}/Co^{3+} in Co-MOF and its composites. The cyclic voltammetry (CV) of the pristine Ni-foam electrode shows that Ni-foam exhibits minute redox activity, and the area under the curve of the bare Ni-foam CV is much smaller than that of the Co-MOF or MOF composite-loaded electrodes (Fig. S3 in the SI). Previous studies revealed a very less specific capacitance of bare Ni-foam, with a specific capacitance of 1.31 F g^{-1},[20,37] Co-MOF-GO composites modified electrode exhibits a higher enclosed area in the CV plot than that of the Co-MOF, as depicted in Fig. 3a. Fig. 3b displays the individual voltammogram of the Co-MOF-GO5-modified electrode at different scan rates, showing the reversible redox behaviour of the electrode material with oxidation and reduction peaks at 0.257 V and 0.17 V, respectively, at a scan rate of 10 mV s^{-1}, conforming to the Co^{2+}/Co^{3+} redox cycle. The steady increase in current with increasing scan rate indicates the highly reversible nature of the electrode material. The specific capacitance values for the Co-MOF, Co-MOF-GO5, and Co-MOF-GO10 electrodes are determined based on their GCD curves and compared, as illustrated in Fig. 3c. The Co-MOF-GO5 composite's GCD curves at diverse current densities are shown in Fig. 3d. The nature of the CV and GCD clearly indicates the

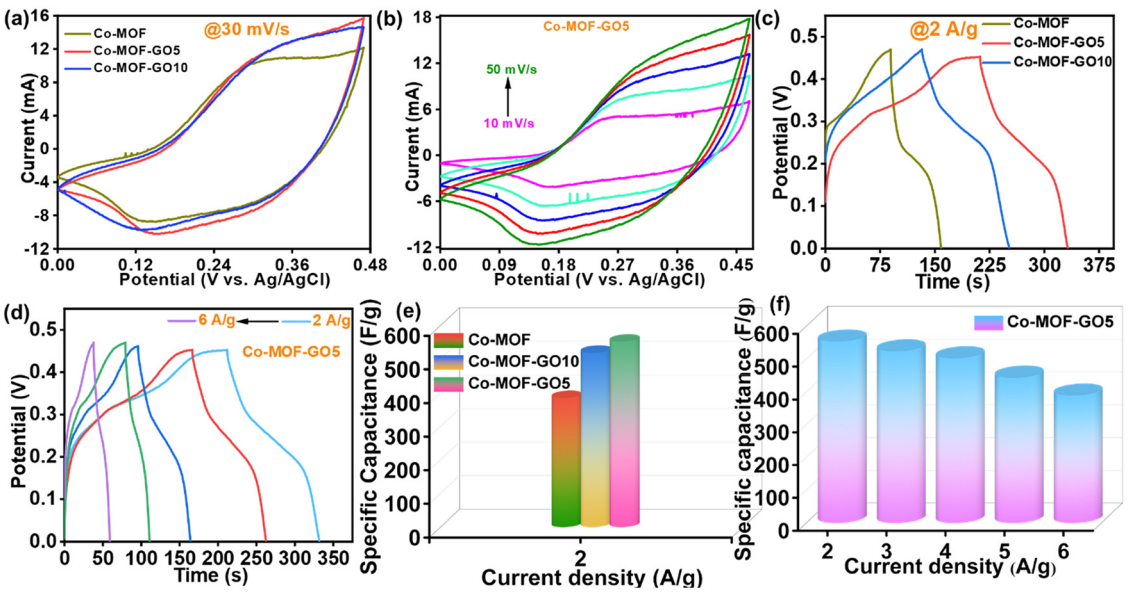

Fig. 3 (a) Comparison of the CV curves of Co-MOF, Co-MOF-GO5, and Co-MOF-GO10 at a scan rate of 30 mV s^{-1} in a three-electrode system. (b) CV curves of Co-MOF-GO5 at different scan rates from 10 mV s^{-1} to 50 mV s^{-1}. (c) Comparison of the GCD plots of Co-MOF, Co-MOF-GO5, and Co-MOF-GO10 at 2 A g^{-1}. (d) GCD plots of Co-MOF-GO5 at different current densities from 2 A g^{-1} to 6 A g^{-1}. (e) Relative specific capacitances of all the materials at 2 A g^{-1}. (f) Corresponding specific capacitances of Co-MOF-GO5 at different current densities.

prominent pseudocapacitance behavior of the material although also mixed with the surface double-layer capacitance. The detailed CV and GCD studies of the Co-MOF are shown in Fig. S4 in the SI. Co-MOF-GO5 displays a higher capacitance than the parent Co-MOF and Co-MOF-GO10 at a current density of 2 A g^{-1}. Remarkably, the values of specific capacitance for Co-MOF and Co-MOF-GO10 are measured as 385 F g^{-1} and 519 F g^{-1}, respectively, while the same is determined as 552 F g^{-1} for Co-MOF-GO5 (Fig. 3e). Fig. 3f shows good rate competence with capacitance retention as the current density increases from 2 to 6 A g^{-1}.

According to Dunn's method, the contributions of surface-limited EDLC and diffusion-limited pseudocapacitive behavior to the total storage performance were estimated from CV curves studied at different scan rates.[20,37,51,56] The electrochemical mechanism can be examined using the following equations:

$$i = av^b, \tag{6}$$

$$\log(i) = \log a + b\log(\mathrm{v}) \tag{7}$$

where the peak current is denoted by i, v represents the scan rate, and a and b are adjustable parameters. If $b = 1$, i is linearly correlated with the scan rate, and the overall electrochemical mechanism is controlled by the non-faradaic process on the electrode surface, implying the EDLC behavior of the electrode materials. On the other hand, if i is proportional to the square root of the scan rate ($b = 0.5$), the diffusion of ions controls the electrochemical process, and storage behavior depends on the faradaic pseudocapacitive nature. The capacitive and diffusive involvement of energy storage can be quantitatively resolved using the following equation proposed by Dunn *et al.*, comprising the current response and scan rate:

$$i = k_1 v + k_2 v^{\frac{1}{2}}, \tag{8}$$

$$\frac{k_1 v}{i} + \frac{k_2 v^{\frac{1}{2}}}{i} = 1, \tag{9}$$

where k_1 and k_2 are coefficients and can be calculated from $i/v^{\frac{1}{2}}$ *vs.* the square root of the scan rate plot. In this equation, $k_1 v/i$ denotes the capacitive involvement and $k_2 v^{1/2}/i$ denotes the diffusion-controlled influence.

In the scan-rate-dependent CV studies, the peak current of the Co-MOF-GO5 electrode is linearly correlated with the square root of the scan rate (Fig. 4a), indicating a major extent of pseudocapacitive behavior. Dunn's method was employed for the estimation of the contributions of surface-limited EDLC and the diffusion-limited pseudocapacitive progressions to the total storage behaviour from CV curves.[20,37] The logarithm plot for the anodic or cathodic peak currents *vs.* the logarithm of scan rate shown in Fig. 4b evaluates the primary diffusive nature of the system, as the b value is determined to be ~0.65 from cathodic peak fitting. The k_1 and k_2 values are determined from Fig. 4c, and the EDLC (capacitive) and pseudocapacitive or diffusive contributions are subsequently calculated using eqn (8). The discrete contributions of capacitive and diffusion-controlled pseudocapacitive behaviours at different scan rates are shown in Fig. 4d. From the figures, it is projected that a diffusion-controlled pseudocapacitive mechanism prevails in the energy storage mechanism of Co-MOF-GO5.

The transport properties of the Co-MOF, Co-MOF-GO5, and Co-MOF-GO10 electrodes were inspected using electrochemical

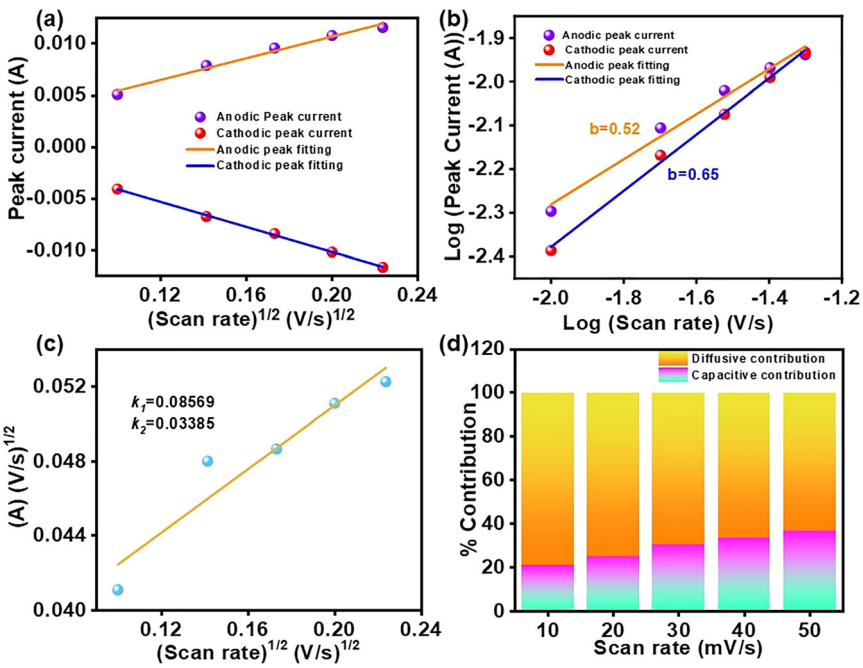

Fig. 4 Mechanistic insights into the charge storage of Co-MOF-GO5. (a) Peak current *vs.* the square root of the scan rate plot. (b) Calculation of the b values from the anodic and cathodic peak-fitting plots. (c) Determination of the k_1 and k_2 values from the $i/v^{1/2}$ plot. (d) Diffusive-capacitive contribution plot.

impedance spectroscopy (EIS). Nyquist plots for the Co-MOF and the composite-modified electrode were obtained over a frequency range from 1 Hz to 10 kHz (Fig. 5a). In the high-frequency region, the plots display semicircles that provide charge transfer resistances (R_{CT}) of 2.33 Ω, 1.2 Ω, and 1.8 Ω for Co-MOF, Co-MOF-GO5, and Co-MOF-GO10, respectively, after fitting in an equivalent circuit given in the inset. The results indicate the lowest resistance during ion transport in Co-MOF-GO5. Furthermore, the Co-MOF, Co-MOF-GO5, and Co-MOF-GO10 composites exhibit different solution resistances (R_S) of 2.64 Ω, 1.4 Ω, and 1.62 Ω, respectively, indicating that Co-MOF-GO5 exhibits the highest relations among the electrolyte and the electrode materials. At lower frequencies, the plots show a straight line, indicating the presence of Warburg impedance. The Warburg impedance phase angle of ~45° in Co-MOF-GO5 reflects better charge transfer and improved ion diffusion likely due to the well-matched Co-MOF and GO combination. This synergy improves electrochemical kinetics and contributes to the superior supercapacitor performance of Co-MOF-GO5.

In a three-electrode configuration, the Co-MOF-GO5 displays a decent energy density of 33 W h kg^{-1} at a power density of 2.9 kW kg^{-1}, as shown in Fig. 5b. This validates the Co-MOF-GO5 electrode's ability to sustain high power and energy densities simultaneously. Moreover, the Co-MOF-GO5-based supercapacitor delivers higher performance than bare Co-MOF and Co-MOF-GO10, maintaining around 80% capacitive retention and achieving 98% coulombic efficiency even after 5000 successive charge–discharge cycles, indicating durable supercapacitive performance (Fig. 5c).[48] For validating the state-of-the-art device, we engineered CR2032 coin cells to show practical, real-world applications. We assembled a symmetric coin cell using Co-MOF-GO5 with equal mass loading in both electrodes. When two fabricated coin cells are connected in series, they can effectively power a light-emitting diode (LED, ~1.8 V) bulb for a few minutes (Fig. 5d). These insights highlight the high potential of Co-MOF-GO5 as a promising material for developing effective energy storage devices for real-world energy applications.

Fig. 6a shows the individual voltammogram of the Co-MOF-GO10-modified electrode at different scan rates, showing the reversible redox behaviour of the electrode material with oxidation and reduction peaks at 0.259 V and 0.172 V, respectively, at a scan rate of 10 mV s^{-1} owing to Co^{2+}/Co^{3+} redox transition when measured in a three-electrode system. The Co-MOF-GO10 composite's GCD curves at diverse current densities are shown in Fig. 6b. The specific capacitance for the Co-MOF-GO10 is measured as 519 F g^{-1} at 2 A g^{-1} current density. Co-MOF-GO10 also reveals a high-rate capability, as it shows only a slight decrease in specific capacitance with increasing current densities (Fig. 6c). The Co-MOF-GO10-based supercapacitor exhibits higher cyclic durability than bare Co-MOF but lower than Co-MOF-GO5 as it maintains around 77% capacitive retention and shows 98% coulombic efficiency after 3300 successive charge–discharge cycles (Fig. 6d). We also calculated the *b*-values and percentage contributions for Co-MOF and Co-MOF-GO10 and compared them with Co-MOF-GO5. It was observed that the bare Co-MOF has the maximum diffusion mechanism and Co-MOF-GO10 has the maximum surface EDLC contribution, while Co-MOF-GO5 has a balanced contribution of EDLC (capacitive) and pseudocapacitive or diffusive contributions between both of them (Fig. 3b, 6a and Fig. S4a, S5). To support the performance of Co-MOF-GO5 compared to pristine Co-MOF and 10% composite, the electrochemically active surface area (ECSA) was measured in the non-faradaic region using cyclic voltammetry. Co-MOF-GO5

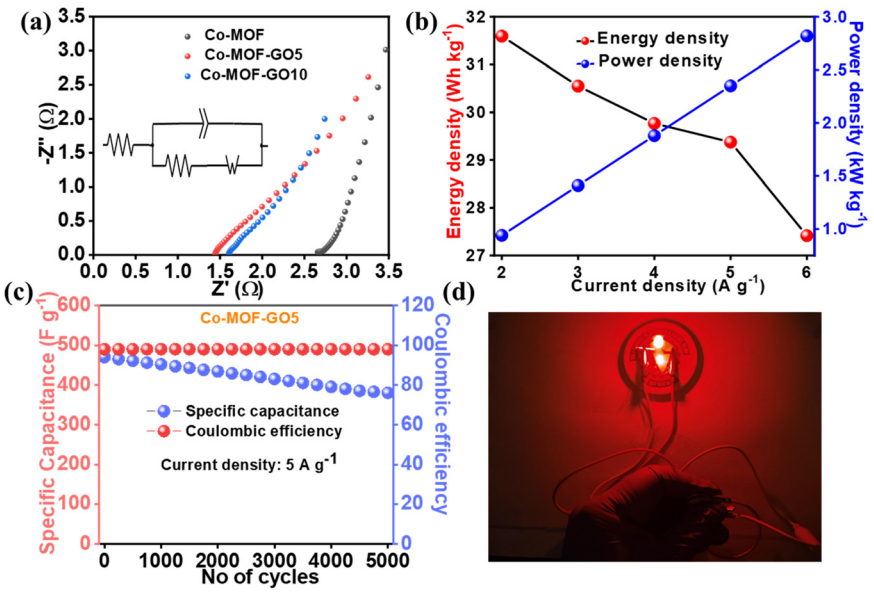

Fig. 5 (a) EIS study of the Co-MOF, Co-MOF-GO5, and Co-MOF-GO10 electrodes (inset: Equivalent circuit). (b) Plots of the energy and power density as a function of the current density. (c) Charge–discharge cycle performance of the Co-MOF-GO5-based supercapacitor for 5000 cycles at a current density of 5 A g^{-1}. (d) Lighting of a light-emitting diode using the two CR2032 coin-cell devices connected in series.

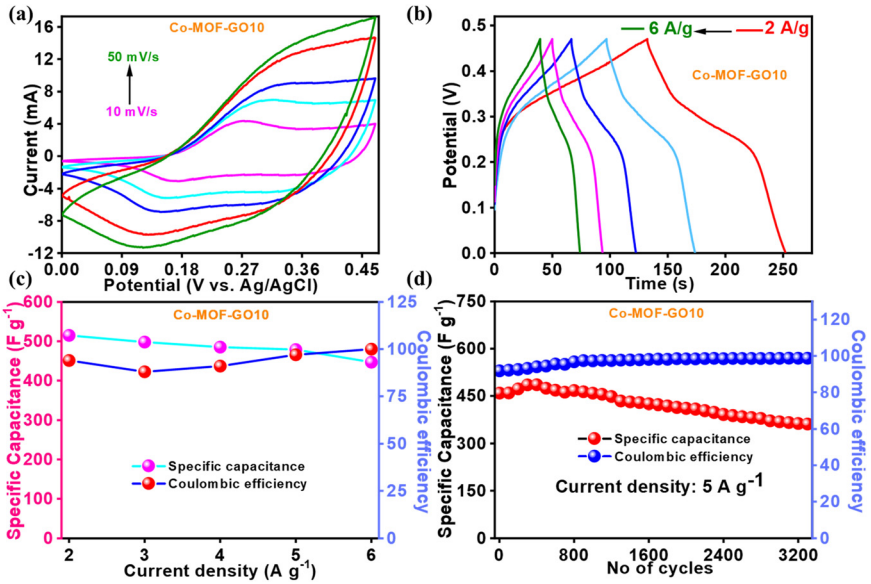

Fig. 6 Supercapacitor performance of Co-MOF-GO10. (a) CV curves of Co-MOF-GO10 at different scan rates from 10 mV s^{-1} to 50 mV s^{-1}. (b) GCD plots of Co-MOF-GO10 at different current densities from 2 A g^{-1} to 6 A g^{-1}. (c) Corresponding specific capacitances and coulombic efficiencies of the Co-MOF-GO10 electrode at different current densities. (d) Charge–discharge cycle performance of the Co-MOF-GO10-based supercapacitor for 3300 cycles at a current density of 5 A g^{-1}.

exhibits an ECSA of 281 cm^2, which is higher than those of pure Co-MOF (96 cm^2) and Co-MOF-GO10 (106 cm^2) (Fig. S6, SI). Pristine Co-MOF exhibits the lowest ECSA due to aggregation, thereby effectively reducing electrochemically accessible active sites. Co-MOF-GO5 achieves the highest ECSA because it contains a moderate amount of GO, which provides an ideal 2D template that prevents Co-MOF aggregation, yielding highly dispersed particles with fully exposed MOF active sites and improved charge transfer. On the other hand, a higher GO loading in the Co-MOF-GO10 sample results in excess GO sheets wrapping around the MOF particles, physically blocking their accessible active sites and reducing the ECSA. Despite the lower ECSA, Co-MOF-GO10 exhibits the highest EDLC due to its higher GO content, demonstrating a storage mechanism based on an electrostatic double-layer arrangement. The synergistic effect of a moderate amount of GO and Co-MOF in Co-MOF-GO5 results in a higher ECSA as well as a CV-enclosed area and specific capacitance that are comparatively better than those of Co-MOF-GO10. Overall, Co-MOF-GO5 exhibits better or comparable energy storage performance compared to recently reported MOFs or MOF-graphene composites, as shown in Table S1 in SI. The synergy of the optimal GO incorporation in Co-MOF-GO5 *via* the *in situ* synthesis process provides better interfacial coupling, faster charge transfer, and the highest ECSA, thereby ameliorating the energy storage properties of Co-MOF-GO5 compared to those of pristine Co-MOF and Co-MOF-GO10.

4. Conclusion

A scalable *in situ* approach was employed with a non-aromatic simple aliphatic succinate-based dicarboxylate linker, inexpensive and commercially accessible precursors, and a water-mediated synthesis route, which resulted in lower synthetic complexity, better scalability, lower cost, and a greener synthesis pathway to integrate GO into a cobalt succinate-based CO-MOF, forming an efficient hybrid electrode for high-performance supercapacitor energy storage by combining diffusion-controlled pseudocapacitance from Co-redox centres and the surface EDLC contribution from GO. The adjusted Co-MOF-GO5 composite delivers a high specific capacitance of 552 F g^{-1} at 2 A g^{-1}, driven by the synergistic interplay among Co^{2+}/Co^{3+} redox activity, GO-enabled charge transport, and the highest ECSA (281 cm^2). Electrochemical impedance analysis reveals reduced charge-transfer resistance and accelerated ion diffusion in Co-MOF-GO5 compared to pristine Co-MOF and higher GO-loaded composites. The electrode delivers an energy density of 33 W h kg^{-1} at a power density of 2.9 kW kg^{-1}, with excellent lateral durability during charging–discharging cycles (~80% retention over 5000 cycles), stabilized through a cooperative heterointerface mechanism. A symmetric CR2032 device based on Co-MOF-GO5 successfully powers a commercial LED, authenticating its practical viability. The findings demonstrate the importance and utility of precisely *in situ*-forming MOF/GO composites to overcome the significant conductivity limitations of MOFs and provide a viable design pathway for high-performance, cost-effective supercapacitor electrodes.

Conflicts of interest

There are no conflicts to declare.

Data availability

The supplementary information (SI) is available. it includes the TGA curves of the Co-MOF and Co-MOF-GO composites and

supporting CV and GCD studies of Co-MOF for supercapacitor parameters. See DOI: https://doi.org/10.1039/d6ma00515b.

Acknowledgements

C. C. acknowledges the Department of Science and Technology, Govt. of India, for providing the instrumental facilities through the PURSE Project No. SR/PURSE/2020/20 (G) at the BITS Pilani Hyderabad Campus. S. K. is thankful to the BITS Pilani Hyderabad Campus for the institutional fellowship and instrumental facilities.

References

1 B. Dunn, H. Kamath and J. M. Tarascon, *Science*, 2011, **334**, 928–935.
2 M. C. Das, S. C. Pal and B. Chen, *Joule*, 2022, **6**, 22–27.
3 N. S. Lewis, *MRS Bull.*, 2007, **32**, 808–820.
4 E. Kabalci, *Energy Convers. Manage.*, 2013, **72**, 51–59.
5 M. Talaat, M. A. Farahat and M. H. Elkholy, *Energy*, 2019, **170**, 668–678.
6 M. Winter and R. J. Brodd, *Chem. Rev.*, 2004, **104**, 4245–4269.
7 Y. Dong, J. Liu, H. Zhang, Q. Li, F. Mao, A. Lu, H. Wu, K. Wang, C. Zhang and Q. Zhang, *SmartMat*, 2023, **4**, 1159.
8 X. Yang, Y. Tian, S. Li, Y.-P. Wu, Q. Zhang, D.-S. Li and S. Zhang, *J. Mater. Chem. A*, 2022, **10**, 12225–12234.
9 S. Xu, J. Wu, X. Wang and Q. Zhang, *Chem. Sci.*, 2023, **14**, 13601–13628.
10 K. Wang, Z. Wang, J. Liu, C. Li, F. Mao, H. Wu and Q. Zhang, *ACS Appl. Mater. Interfaces*, 2020, **12**, 47482–47489.
11 C. Choi, D. S. Ashby, D. M. Butts, R. H. DeBlock, Q. Wei, J. Lau and B. Dunn, *Nat. Rev. Mater.*, 2020, **5**, 5–19.
12 Y. Liang and Y. Yao, *Nat. Rev. Mater.*, 2023, **8**, 109–122.
13 K. Padmasri, S. Khan, S. A. Singh, C. Chakraborty and P. Doddipatla, *ACS Omega*, 2026, **11**, 23480–23489.
14 Y. Ma, X. Xie, W. Yang, Z. Yu, X. Sun, Y. Zhang, X. Yang, H. Kimura, C. Hou, Z. Guo and W. Du, *Adv. Compos. Hybrid Mater.*, 2021, **4**, 906–925..
15 P. Naskar, A. Maiti, P. Chakraborty, D. Kundu, B. Biswas and A. Banerjee, *J. Mater. Chem. A*, 2021, **9**, 1970–2017.
16 L. L. Zhang and X. S. Zhao, *Chem. Soc. Rev.*, 2009, **38**, 2520–2531.
17 T. Wang, X. Zang, X. Wang, X. Gu, Q. Shao and N. Cao, *Energy Storage Mater.*, 2020, **30**, 367–384.
18 A. M. Bryan, L. M. Santino, Y. Lu, S. Acharya and J. M. D'Arcy, *Chem. Mater.*, 2016, **28**, 5989–5998.
19 C. Yuan, H. B. Wu, Y. Xie and X. W. Lou, *Angew. Chem., Int. Ed.*, 2014, **53**, 1488–1504.
20 S. Khan, S. Chand, P. Sivasakthi, P. K. Samanta and C. Chakraborty, *Small*, 2024, **20**, 2401102.
21 S. Khan, S. Chand, P. Thippeswamy, D. Ghosh and C. Chakraborty, *Sustainable Energy Fuels*, 2025, **9**, 2698–2706.
22 H. C. Zhou, J. R. Long and O. M. Yaghi, *Chem. Rev.*, 2012, **112**, 673–674.
23 H. C. Zhou and S. Kitagawa, *Chem. Soc. Rev.*, 2014, **43**, 5415–5418.
24 G. Chakraborty, I. H. Park, R. Medishetty and J. J. Vittal, *Chem. Rev.*, 2021, **121**, 3751–3891.
25 J. Liu, X. Song, T. Zhang, S. Liu, H. Wen and L. Chen, *Angew. Chem., Int. Ed.*, 2021, **60**, 5672–5687..
26 X. Xiao, S. Tao, H. Lian, Y. Tian, W. Deng, H. Hou, G. Zou and X. Ji, *ACS Nano*, 2024, **18**, 28444–28455.
27 D. Feng, T. Lei, M. R. Lukatskaya, J. Park, Z. Huang, M. Lee, L. Shaw, S. Chen, A. A. Yakovenko, A. Kulkarni and J. Xiao, *Nat. Energy*, 2018, **3**, 30–36.
28 M. Zhao, Y. Wang, Q. Ma, Y. Huang, X. Zhang, J. Ping, Z. Zhang, Q. Lu, Y. Yu, H. Xu and Y. Zhao, *Adv. Mater.*, 2015, **27**, 7372–7378.
29 S. Khan, A. Biswas, S. Chand and C. Chakraborty, *Chem. Commun.*, 2026, **62**, 9477–9480.
30 S. Halder, A. K. Pradhan, S. Khan and C. Chakraborty, *Energy Adv.*, 2023, **2**, 1713–1723.
31 A. Husain, N. Hussain and S. M. Mobin, *J. Mater. Chem. A*, 2026, **14**, 8351–8360.
32 K. Chen, X. L. Wang, W. Hu, Q. Kong, H. Pang and Q. Xu, *Small Struct.*, 2022, **3**, 2100200.
33 Z. Xia, X. Jia, X. Ge, C. Ren, Q. Yang, J. Hu, Z. Chen, J. Han, G. Xie, S. Chen and S. Gao, *Angew. Chem.*, 2021, **133**, 10316–10327..
34 F. L. Li, P. Wang, X. Huang, D. J. Young, H. F. Wang, P. Braunstein and J. P. Lang, *Angew. Chem., Int. Ed.*, 2019, **58**, 7125–7129..
35 F. B. Ajdari, E. Kowsari, M. N. Shahrak, A. Ehsani, Z. Kiaei, H. Torkzaban, M. Ershadi, S. K. Eshkalak, V. Haddadi-Asl, A. Chinnappan and S. Ramakrishna, *Coord. Chem. Rev.*, 2020, **422**, 213441.
36 S. J. Shin, J. W. Gittins, C. J. Balhatchet, A. Walsh and A. C. Forse, *Adv. Funct. Mater.*, 2024, **34**, 2308497.
37 S. Khan, S. Chand and C. Chakraborty, *Chem. Eng. J.*, 2025, **516**, 164232.
38 Q. Liu, Z. Guo, C. Wang, S. Guo, Z. Xu, C. Hu, Y. Liu, Y. Wang, J. He and W. Y. Wong, *Adv. Sci.*, 2023, **10**, 2207545.
39 R. Sahoo, S. Ghosh, S. Chand, S. C. Pal, T. Kuila and M. C. Das, *Compos. Part B Eng.*, 2022, **245**, 110174.
40 Z. Xia, *et al.*, *Angew. Chem.*, 2021, **133**, 10316–10327..
41 S. Ramesh, S. Khandelwal, K. Y. Rhee and D. Hui, *Composites, Part B*, 2018, **138**, 45–54.
42 P. Srimuk, S. Luanwuthi, A. Krittayavathananon and M. Sawangphruk, *Electrochim. Acta*, 2015, **157**, 69–77.
43 S. Gautam, S. Rialach, S. Paul and N. Goyal, *RSC Adv.*, 2024, **14**, 14311–14339.
44 V. Jabbari, J. M. Veleta, M. Zarei-Chaleshtori, J. Gardea-Torresdey and D. Villagrán, *Chem. Eng. J.*, 2016, **304**, 774–783.
45 C. C. Hou, L. Zou, Y. Wang and Q. Xu, *Angew. Chem., Int. Ed.*, 2020, **59**, 21360–21366.
46 P. Zhang, B. Y. Guan, L. Yu and X. W. Lou, *Angew. Chem.*, 2017, **129**, 7247–7251.
47 M. Du, D. Song, A. Huang, R. Chen, D. Jin, K. Rui, C. Zhang, J. Zhu and W. Huang, *Angew. Chem.*, 2019, **131**, 5361–5366..
48 S. Khan, S. Halder, S. Chand, A. K. Pradhan and C. Chakraborty, *Dalton Trans.*, 2023, **52**, 14663–14675.
49 C. Livage, C. Egger and G. Férey, *Chem. Mater.*, 2001, **13**, 410–414.

50 S. Khan, A. K. Shukla, A. Bhattacharya, S. Chand and C. Chakraborty, *Inorg. Chem.*, 2024, **63**, 18438–18447.
51 T. M. Gür, *Energy Environ. Sci.*, 2018, **11**, 2696–2767.
52 Z. Xia, *et al.*, *Angew. Chem.*, 2021, **133**, 10316–10327..
53 R. Abazari, S. Sanati, A. Morsali, A. Slawin and C. L. Carpenter-Warren, *ACS Appl. Mater. Interfaces*, 2019, **11**, 14759–14769..
54 F. Cao, M. Zhao, Y. Yu, B. Chen, Y. Huang, J. Yang, X. Cao, Q. Lu, X. Zhang, Z. Zhang and C. Tan, *J. Am. Chem. Soc.*, 2016, **138**, 6924–6927.
55 R. Abazari, *et al.*, *ACS Appl. Mater. Interfaces*, 2019, **11**, 14759–14769..
56 S. Pervez and M. Z. Iqbal, *Small*, 2023, **19**, 2305059.